UNIVERSITÀ DEGLI STUDI DI PADOVA

Dipartimento di Fisica e Astronomia "Galileo Galilei"

Corso di Laurea in Fisica

Tesi di Laurea

Measuring the performance of a reversed kerr traveling-wave parametric amplifier for quantum sensing in axion dark matter search

Relatore

Prof. Caterina Braggio

Correlatore

Dr. Giuseppe Ruoso

Laureando

Pietro Borghi

Anno Accademico 2021/2022

Contents

Introduction

Quantum processors harness the intrinsic properties of quantum mechanical systems - such as quantum parallelism and quantum interference - to solve certain problems where classical computers fall short. Over the past few decades, rapid developments in the science and engineering of quantum systems have advanced the frontier in quantum computation, from the realm of scientific explorations on single isolated quantum systems toward the creation and manipulation of multiqubit processors.

In superconducting quantum computing, in particular, qubit state information is conveyed via low-power microwave fields [1, 2]. As such, ultralow-noise microwave amplification plays a central role in measuring these fields to quickly and accurately infer the qubit state. Parametric amplifiers based on Josephson junctions and approaching 'quantum-limited' noise performance have become one of the leading technologies to this task. Usually, these devices are co-located close to qubits and related circuitry at the lowest temperature stage ($T = 10-20$ mK) of a dilution refrigerator cryostat, and are followed by a standard low-noise cryogenic high-electron-mobility-transistor (HEMT) amplifier at the $T = 3-4$ K stage, where their high dissipation is not an issue (see Fig. 1).

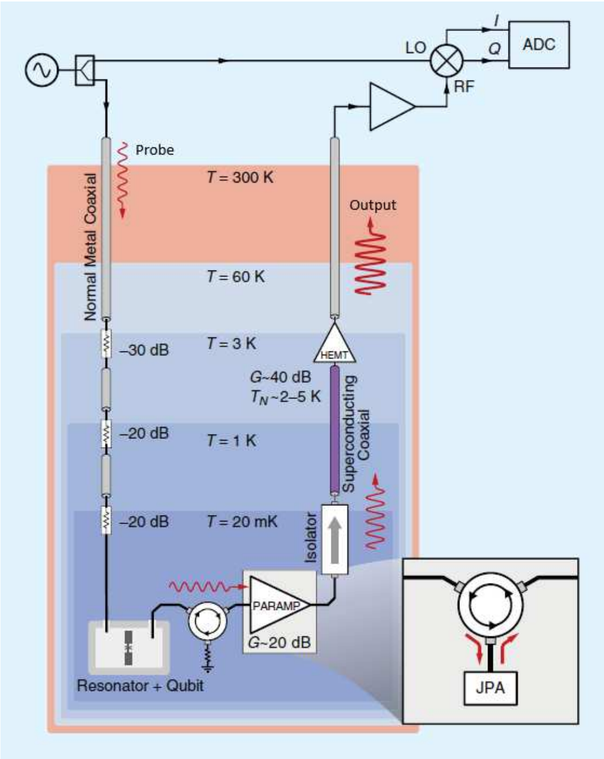

Figure 1: Schematic of the experimental setup used for dispersive qubit readout [1]. A Josephson parametric amplifier (JPA) is employed at the lowest temperature stage, next to the qubit circuit.

Even more performing ultralow-noise receiver electronics is required to readout 3D microwave resonators in dark matter search at haloscopes, detectors that probe the existence of axions in the galactic halo. In this case, exceedingly small powers, in the order of $10^{-23} - 10^{-24}$ W at ~ 10 GHz frequencies need to be measured with great accuracy. The sensitivity of these experiments is strongly related to the overall noise temperature of the system, mainly determined by the noise introduced by the first stage of amplification.

In addition, haloscopes are required to scan the most plausible axion-photon interaction parameter space over a broad range of masses (frequencies), which translates into the necessity of employing amplifiers with $\sim$ GHz bandwidths. Josephson traveling wave parametric amplifiers (JTWPAs) provide the specifications that are required in dark matter search, besides being set to become a ubiquitous tool in most of superconducting quantum information research efforts.

This thesis focuses on the characterization of a JTWPA-based amplification chain, performed on QUAX's haloscope [3] at INFN's National Laboratories of Legnaro. The first chapter is dedicated to describing the functioning of parametric amplifiers, with specific focus on JTWPAs. Then, a brief overview on axions and axion search at haloscopes is provided. Finally, the last chapter reports the experimental measurements performed toward the characterization of the studied amplification chain, along with the obtained results.

Nel campo dell'informazione e del calcolo quantistico a qubit superconduttori, l'utilizzo di amplificatori a bassissimo rumore risulta di fondamentale importanza nella lettura dello stato dei qubit, che avviene attraverso la misura di segnali di debolissima intensità nello spettro delle microonde. Una tecnologia particolarmente adatta a questo scopo è quella degli amplificatori parametrici a giunzioni Josephson (JPAs). Questi dispositivi vengono solitamente collocati nelle vicinanze dei qubit nello stadio a temperatura più bassa (T = 10 - 20 mK) di un refrigeratore a diluizione e sono spesso seguiti da tradizionali amplificatori HEMT (high electron mobility transistor) criogenici collocati nello stadio a temperatura T = 3 - 4 K.
Amplificatori ancora più prestazionali sono richiesti nell'ambito della ricerca della materia oscura mediante gli aloscopi, rivelatori che si occupano di sondare la possibile esistenza degli assioni. In questo caso, il sistema fisico posto in ingresso all'amplificatore è una cavità tridimensionale a microonde con frequenza di risonanza intorno ai 10 GHz e la potenza attesa per il segnale da rivelare è dell'ordine di 10^{-23} – 10^{-24} W. La sensibilità di questi esperimenti è fortemente legata alla temperatura di rumore complessiva dell'intero sistema, che a sua volta è determinata principalmente dal rumore introdotto nel primo stadio della catena amplificazione.
Inoltre, poiché gli aloscopi sono progettati in modo da poter sondare lo spazio dei parametri dell'interazione assione - fotone su un ampio range di masse (frequenze), essi necessitano l'utilizzo di amplificatori con bande passanti dell'ordine di qualche GHz. L'amplificatore parametrico Josephson traveling-wave (JTWPA), dispositivo sempre più spesso impiegato nel campo dell'informazione e del calcolo quantistico, risponde a queste esigenze.
L'obiettivo di questa tesi è la caratterizzazione della catena di amplificazione utilizzata per la lettura dell'aloscopio dell'esperimento QUAX, presente presso i Laboratori Nazionali di Legnaro e in cui è un JTWPA è impiegato come preamplificatore.

Chapter 1

Parametric Amplification and TWPAs

1.1 Gain, Bandwidth, Noise, and Standard Quantum Limit

An amplifier is a device designed to amplify an input signal, possibly on a large frequency span and with little distortion or added noise. Before getting into the specifics of what a parametric amplifier, and in particular a TWPA is, let us briefly go through a (non-exhaustive) list of figures of merit which will be extensively used in the rest of this thesis.

The most fundamental feature when characterizing an amplifier is, obviously, the gain. Seen as a transfer function with a signal amplitude A_{in} at the input and a signal amplitude A_{out} at the output, the power gain factor G is defined as the output to input amplitude ratio: $\sqrt{G} = A_{out}/A_{in}$.

Since gain G is a function of signal frequency ω_s, we must also define an amplifier's bandwidth Δ_{bw} as the frequency range where $G(\omega_s)$ is higher than a defined threshold value, usually $G_{max}/2$ in linear units, or $G_{max} - 3\text{dB}$ in decibels.

Finally, another critical parameter for an amplifier is noise power, which ultimately provides a threshold for signal readout and detection.
During the process of amplification, noise may arise from multiple sources, both environmental and intrinsic to the amplifier. Regardless of the actual source, noise can always be modeled in terms of an equivalent thermal noise source and characterized with an equivalent noise temperature, given by:

$$T_n = \frac{N}{k_B B} \tag{1.1}$$

where N is noise power, k_B is Boltzmann's constant and B is some fixed bandwidth, generally the operational bandwidth of the component or system [4].
In presence of a set of cascaded amplifiers, the equivalent noise temperature of the entire amplification chain T_{amp} can be expressed in terms of the individual gain figures G_i and the equivalent noise temperatures $T_{n,i}$ associated to each constituent as:

$$T_{amp} = T_{n,1} + \frac{T_{n,2}}{G_1} + \frac{T_{n,3}}{G_1 G_2} + \cdots \tag{1.2}$$

In this thesis, we will often refer to T_{amp} as 'equivalent *receiver* noise temperature'.
From Eq. 1.2 we see that T_{amp} is dominated by the noise contribution from the first amplifier in the chain, whereas the gain of the first amplifier has the effect of suppressing the noise from the second amplifier, and so on. The employment of ultralow-noise amplifiers, such as TWPAs, and in general parametric amplifiers, as the earliest stage in amplification chains is, therefore, essential in reaching the extremely low noise temperatures required to readout both qubits and haloscope cavities.

For frequencies f in the microwave domain, at room temperature ($k_B T \gg hf$) noise power is typically dominated by thermal, or 'Johnson', noise, caused by thermal vibration of bound charges. Thermal fluctuations can, however, be reduced to a minimum by working in a cryogenic environment

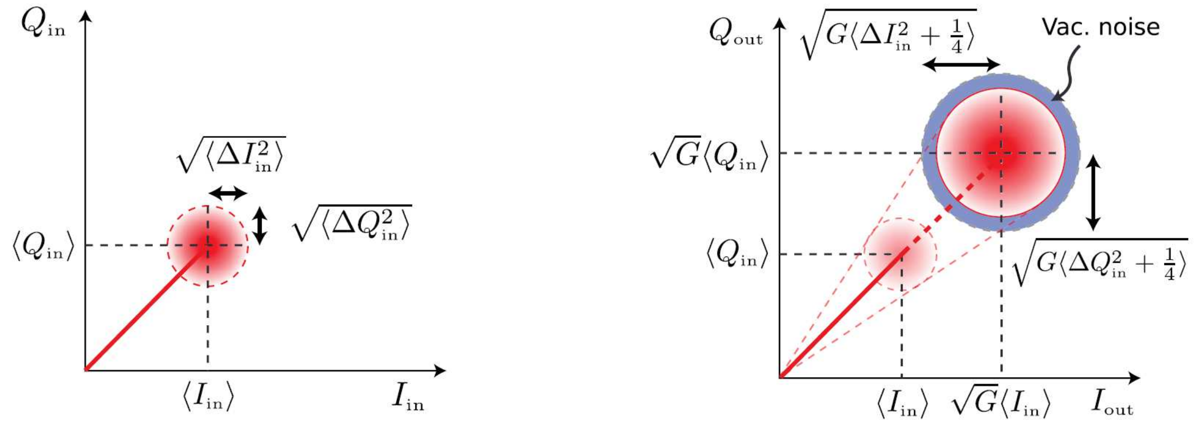

(a) Amplifier input

(b) Amplifier output

Figure 1.1: Schematic illustration of a quantum-limited, phase preserving amplification process [2]. (a) The input state $a_{in} = I_{in} + Q_{in}$ is centered at $(\langle I_{in} \rangle, \langle Q_{in} \rangle)$ and has a noise represented by the radii of the circles along the real and imaginary axes. (b) In the output state both quadratures get amplified by a factor $\sqrt{G}$, while half photon of noise gets added (in blue).

$(k_B T \lesssim hf)$. This is usually achieved by means of ^{3}He-^{4}He dilution refrigeration technology.
In these conditions, a lower limit on the noise performance of an amplifier is set by quantum fluctuations. In fact, if we consider an amplifier where the input and the output signals are quantum fields, and they thus obey to the commutation relations:

$$\left[a_{in}, a_{in}^{\dagger}\right] = \left[a_{out}, a_{out}^{\dagger}\right] = 1 \tag{1.3}$$

it can be shown ('Caves theorem' [5]) that the ideal relation $a_{out} = \sqrt{G} a_{in}$ cannot hold. Rather, to satisfy Eq. 1.3 another, at least one, internal mode must be taken into account. This internal mode is also described by its quantum operator b, fulfilling $\left[b, b^{\dagger}\right] = 1$, and is commonly called 'idler' mode, as a legacy of earlier work in nonlinear optics - the connection to nonlinear optics will become clearer in the next section. The relation between input and output fields thus becomes:

$$a_{out} = \sqrt{G} a_{in} + \sqrt{G-1} b_{in}^{\dagger} \tag{1.4}$$

finally complying with Eq. 1.3.
As an immediate consequence, the noise spectral density at the output of the amplifier N_{out} is the sum of two contributions, one from the noise incident at the signal frequency, and the other from the idler frequency:

$$N_{out} = G N_{in,s} + (G-1) N_{in,id} \tag{1.5}$$

where $N_{in,s}$ and $N_{in,id}$ are the signal and idler input noises respectively.

The noise added by the amplification process, i.e. $N_{in,id}$, thus, directly arises from the idler mode and has a minimum value equal to $N_{in,id} = hf/2$, set by quantum 'zero-point' fluctuations of the environment. This limit is often referred to as 'Standard Quantum Limit' (SQL) and the corresponding noise power as 'half-photon of noise'.

However, since quantum fluctuations also set a minimum value, equal to $N_{in,s} = hf/2$, for the input noise at the signal frequency, an alternative definition of SQL is frequently adopted, accounting for noise contributions both at signal and idler frequencies. In terms of equivalent noise temperatures, this corresponds to the definition an 'equivalent *system* noise temperature' given by:

$$T_{sys} = T_{in} + T_{amp} \tag{1.6}$$

where $T_{in} = N_{in,s}/k_B B$ is the signal input noise temperature, directly related to the physical temperature of the thermodynamic bath at the input of the amplifier, while T_{amp} is the equivalent *receiver*

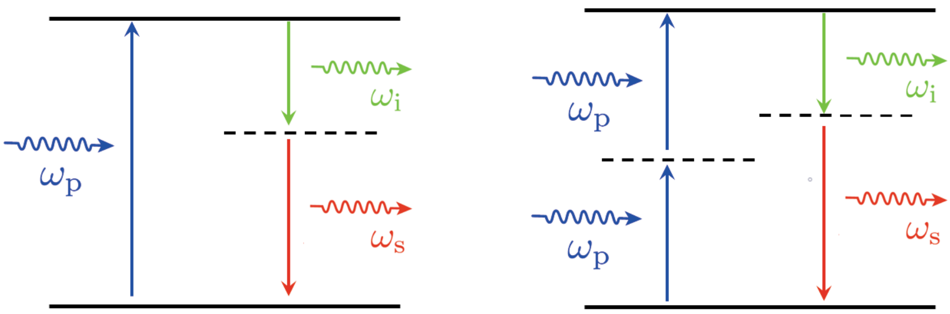

(a) Three-wave mixing (3WM) (b) Four-wave mixing (4WM)

Figure 1.2: Energy diagrams for 3WM and 4WM processes.
(a) One pump photon at ω_p gets down-converted into a signal and an idler photon, at frequencies ω_s and ω_p respectively. (b) Two pump photons at frequency ω_p are converted into a signal and an idler photon, at frequencies ω_s and ω_p.

noise temperature defined in Eq. 1.2.
Adopting these conventions, SQL is thus defined as 'one photon of noise', and corresponds to a system noise temperature given by $T_{sys} = hf/k_B$. This must be interpreted as the minimum possible noise power at the output of an amplifier or amplification chain; whereas 'half photon' is the minimum possible noise power *added* by an amplifier.

The process we have so far described, as a whole, is known as 'phase-preserving' or 'phase-insensitive' amplification. A 'phase-sensitive' amplification is also possible, but will not be discussed in this thesis. Figure 1.1 illustrates phase-preserving amplification in the phase-space.

1.2 Wave Mixing and Parametric Amplification

Although most of the current interest in the field is motivated by applications in superconducting quantum computing, the concepts of parametric amplification are actually quite old, and are employed not only in electronic systems, but also in optical and, originally, mechanical ones. In particular, parametric amplification naturally emerges and is easily understood as a consequence of wave-mixing processes in nonlinear optics [6].

Generalizing the well-known relation $P(t) = \epsilon_0 \chi^{(1)} E(t)$, the induced polarization $P(t)$ in a nonlinear medium can be expressed as a power series in the electric field strength $E(t)$ as:

$$P(t) = \epsilon_0 \left[\chi^{(1)} E(t) + \chi^{(2)} E^2(t) + \chi^{(3)} E^3(t) + \dots \right] \tag{1.7}$$

where ϵ_0 is the permittivity of free space and $\chi^{(i)}$ is the ith-order nonlinear susceptibility.

The simplest case in which amplification may arise from optical waves in a nonlinear medium, is given by a second-order nonlinear medium with an incident electric field consisting of two parts: a *pump* at frequency ω_p with amplitude E_p, and a *signal* at frequency ω_s with amplitude E_s. Such input field can be written as:

$$E(t) = E_p e^{(-i\omega_p t)} + E_s e^{(-i\omega_s t)} + c.c. \tag{1.8}$$

where *c.c.* denotes complex conjugate. Inserting this expression in the second-order term of Eq. 1.7 results in a nonlinear polarization consisting of contributions at frequencies 0, $2\omega_p$, $2\omega_s$, $\omega_p + \omega_s$ and $\omega_p - \omega_s$. Among the four non-zero frequency components that are present, the one allowing parametric amplification is the latter, produced in the so-called 'difference-frequency generation' process.
As in fact shown by the photon energy-level diagram sketched in Fig. 1.2a, the conservation of energy in the process requires that for every photon that is created at the difference frequency $\omega_i = \omega_p - \omega_s$,

known as the *idler* frequency, a photon at ω_p must be destroyed and a photon at ω_s must be created. In other words, energy gets transfered from the pump frequency mode ω_p, to the signal frequency mode ω_s via the creation of a third mode ω_i. As three photons are involved, this process is also known as 'three wave mixing' (shorted as 3WM).

Quite similar to 3WM, but arising in media which have a third-order ('Kerr') nonlinearity, is 'four wave mixing' (shorted as 4WM) in which two pump photons give one signal and one idler photon, obeying the energy conservation relation $2\omega_p = \omega_s + \omega_i$. Fig. 1.2b illustrates the energy diagram for this second variation of parametric amplification.

Finally, both 3WM and 4WM processes can be further subdivided, depending on whether the signal mode frequency ω_s and the idler mode frequency ω_i are or are not the same: if $\omega_s = \omega_i$ the amplification is said to be 'degenerate'; otherwise it is said to be 'non-degenerate'.

The amplifier presented in this thesis exploits a four wave mixing, non-degenerate parametric process.

1.3 Josephson junctions and Josephson based amplifiers

As we have seen, a fundamental prerequisite to parametric amplification is the availability of a non-linear medium or element, allowing wave mixing processes - either 3WM or 4WM - to happen. In electronics, and specifically in the microwave domain, the role of the non-linear medium is often played by a non-linear inductance. Although other designs are also possible [7], this is typically achieved by means of Josephson junctions.
Since this is also the case for the traveling-wave amplifier which we will be studying, we have though it useful to give a brief overview on Josephson junctions and on Josephson based amplification in general.

A Josephson junction (JJ) [8] consists of two superconducting electrodes separated by a thin insulating barrier. If the barrier is thin enough, superconducting charge carriers (Cooper-pairs) can quantum-mechanically tunnel through the barrier, generating a supercurrent I flowing without any applied voltage. The process, known as 'Josephson effect', is described by the equations

$$I = I_c \sin\phi \qquad\qquad V = \frac{\hbar}{2e}\frac{d\phi}{dt} \tag{1.9}$$

relating the voltage V and current I across the junction to a critical current I_c, determined by material properties, and to gauge-invariant phase difference between the two electrodes ϕ. Taken together, these equations imply that a Josephson junction can be modeled as a nonlinear inductor with inductance

$$L_J(I) = \frac{L}{\sqrt{1-(I/I_c)^2}} \tag{1.10}$$

with $L = \hbar/2eI_c$ being the linear inductance of the junction.

In superconducting quantum circuits, Josephson junctions are often employed in the so-called superconducting quantum interference device (SQUID) topology, consisting of two, usually identical, junctions in a ring configuration (see Fig. 1.3a).
By threading the ring loop with an external DC magnetic flux Φ_{dc}, due to a magnetic flux constraint on superconducting rings, the SQUID inductance becomes a periodic function of the flux:

$$L_{squid}(I, \Phi_{dc}) = \frac{L_J(I)}{2\cos(\pi\Phi_{dc}/\Phi_0)} \tag{1.11}$$

where $\Phi_0 = h/2e$ is the magnetic flux quantum.
As a result, the SQUID can overall be modeled as a flux-tunable Josephson junction, with inductance L_{squid}.

Notably, an array of SQUIDs was the main constituent of the resonant Josephson Parametric Amplifier (JPA) implemented in 2007 by Castellanos-Beltran et al. [9]. After they experimentally recorded,

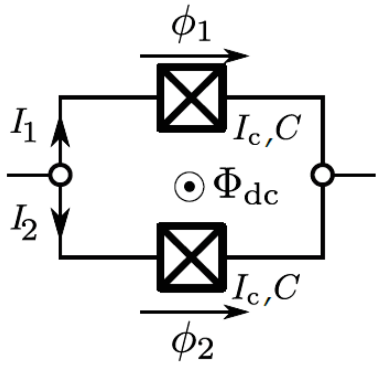

(a) The SQUID

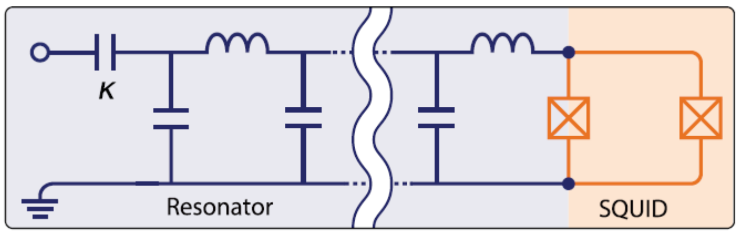

(b) A Josephson Parametric Amplifier

Figure 1.3: Circuit schematic of a symmetric SQUID and of a JPA. (a) Two identical Josephson junctions, represented by the two crosses, are in parallel in a superconducting loop. The loop is threaded with an external DC magnetic flux Φ_{dc}. (b) A quarter-wavelength resonator (blue) is shorted to ground via a SQUID (orange). Parametric amplification can be achieved by applying a pump in two different ways: either by modulating the current through the junctions or by modulating the flux bias at GHz frequencies.

one year later, quantum-limited noise performance while having more than 20 dB of power gain [10], their device became an established model for resonant JPAs, to the point of being often regarded as the first present Josephson amplifier, although some pioneering work on the subject had been already carried out by Bernard Yurke in the late 1980's [11, 12].
Since then, resonant JPAs reaching SQL have been successfully demonstrated and operated in numerous labs, and remarkable progresses have been obtained regarding their bandwidth, saturation points, pumping schemes, frequency tunability and directionality.

Apart from the specifics of each implementation, all these devices share the common idea of enhancing the parametric interactions, essential to amplification, by placing the nonlinear Josephson element into an LC resonator (Fig. 1.3b). This, in fact, allows for a prolonged interaction time between the pump and the signal via the nonlinearity, and thus for a greater power gain.
At the same time, the resonating mechanism puts a serious constraint on the amplification bandwidth, which decreases as the time spent by the signal inside the resonator increases. More precisely, it can be shown that the product $\Delta_{bw}\sqrt{G_{max}}$ is approximately a constant for a resonant amplifier.

This clashes with the contemporary paradigm of scalability and represents a significant limitation for some applications, for instance frequency multiplexed readout of a high number of qubits. Also, this is clearly incompatible with the need of scanning the largest possible frequency range at haloscopes. Recently, this limitation has been overcome by traveling wave parametric amplifiers (TWPAs), consisting of non-resonant nonlinear transmission lines, exhibiting an amplification bandwidth up to a few GHz. The next section is dedicated to describing the functioning of such a device.

1.4 Traveling Wave Amplification

We have seen that in resonant amplification the interaction time between the signal and the non linear medium is increased by placing the nonlinear medium in a cavity. In traveling wave amplification, instead, the same interaction time is optimized by increasing the physical length of the nonlinear medium.
In a microwave equivalent of nonlinear optical fibers (NOFs) [13], in a TWPA the signal gets amplified as it propagates along the nonlinear medium (Fig. 1.4b), thus removing the fundamental gain-bandwidth constraint typical of resonant amplifiers.
The simplest Josephson based implementation of this idea consists in an array of a few hundred identical unit cells, each comprising a nonlinear Josephson inductor and a shunt capacitor to ground, guaranteeing the impedance matching of the amplifier with the typical 50 Ω impedance of the external environment (Fig. 1.4a).

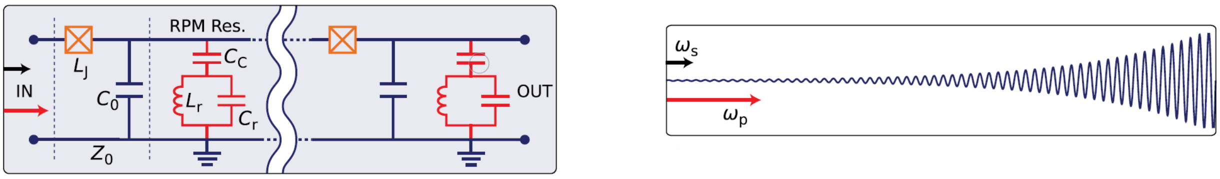

(a) Resonant phase matching in a Josephson TWPA (b) Amplification in a TWPA

Figure 1.4: (a) Simplified circuit representation of a Josephson traveling wave amplifier (JTWPA). The characteristic impedance of each unit cell is set by the in-line Josephson inductor L_J (orange), and the shunt capacitor C_0 (blue). A resonant LC circuit (red) is used to phase match the four-wave amplification process. (b) Schematic of how the signal gets amplified in each unit cell as it propagates through the device.

Albeit naturally overcoming some of the major limitations of resonant JPAs, TWPAs too are not exempt from constraints, the most important of which being phase matching. Whichever the parametric process - either 3WM or 4WM - involved in amplification, in fact, very specific phase matching conditions must hold between the signal, pump and idler fields to obtain maximum gain. These conditions arise from the solution of the coupled mode equations (CMEs) describing the propagation of the fields along the nonlinear medium, and can be understood as a direct consequence of momentum conservation.

Typically, the problem of phase matching is solved by means of so-called 'dispersion engineering', consisting in engineering a distortion in the dispersion relation of the transmission line. This can be achieved by either using a photonic-crystal like approach, in which a photonic gap is opened in the dispersion relation by periodically modulating the transmission line [14], or a resonant phase matching approach, in which a stop band gap is created in the dispersion relation by introducing resonators at periodic intervals along the transmission line [15, 16].
Dispersion engineered TWPAs, however, suffer from two main disadvantages. First, the presence of the gap in the dispersion relation typically produces a discontinuous amplification band with significant ripples in the gain profile. Secondly, optimal amplification is guaranteed only when the TWPA is pumped at a designed frequency, causing the amplification band to be fixed by design.
To overcome these difficulties, a novel approach to phase matching, based on the sign reversal of the Kerr third-order nonlinearity and with no need for dispersion engineering, has recently been proposed [17]. Since the amplifier which is the subject of this thesis features this new 'reversed Kerr' phase matching approach, the last section of this chapter is dedicated to describing how this is implemented in practice.

1.5 The reversed Kerr TWPA

The studied device is the result of the past few years of work of the 'TWPA team' at the Neel Institute in Grenoble. A thorough description of reversed Kerr phase matching mechanisms and of the device fabrication details, along with a demonstration of typical device performances can be found in [18]. We summarize here the main characteristics.

The device consists of 700 cells spanning 6 mm, with each cell containing a superconducting loop with three large - high critical current I_0 - and one small - low critical current rI_0 - Josephson junctions in either arm (Fig 1.5a). This design, practically an asymmetric SQUID, is known with the name of superconducting nonlinear asymmetric inductive element (SNAIL) [19], and has also been adopted for 3WM resonant parametric amplification [20–22] and in the implementation of Kerr-cat qubits [23].
The asymmetry between the two arms of the superconducting loop allows to have both second-order and third-order nonlinear terms in the Taylor expansion of the current-phase relation:

$$I(\phi) \approx \frac{\Phi_0}{2\pi L}\phi - 3\Phi_0\sqrt{\frac{R_Q}{\pi^3 Z^3}}g_3\phi^2 - 4\Phi_0\frac{R_Q}{\pi^2 Z^2}g_4\phi^3 \tag{1.12}$$

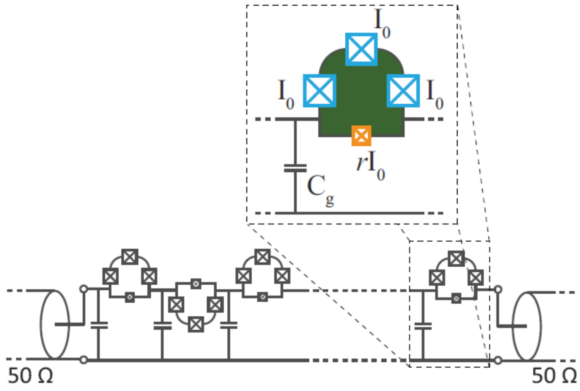

(a) Schematic of the reversed Kerr TWPA

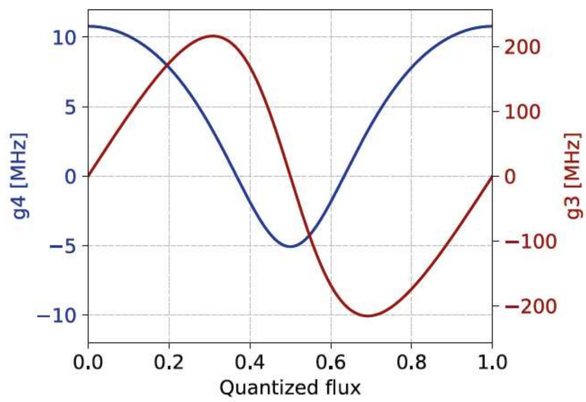

(b) g_3 and g_4 dependence on external magnetic flux

Figure 1.5: Reversed Kerr TWPA implementation.
(a) Circuit schematic of the TWPA: each unit cell comprises 4 Josephson junctions (3 large, with critical current I_0, and one smaller, with critical current rI_0) forming a SNAIL, and a ground capacitance C_g. Adjacent SNAIL cells have opposite physical orientation, and thus inverted magnetic flux polarity, to further suppress spurious 3WM processes. In this fashion, since g_3 is an odd function of external flux (see (b)), its value in adjacent cells has opposite sign, resulting in an overall cancellation of 3WM processes at the wavelength scales under discussion.
(b) Nonlinear coefficients g_3 and g_4 as a function of external magnetic flux. The operating point of the device, for what concerns this thesis, is around 0.5 in the displayed scale ('half flux' condition).

where g_3 and g_4 are respectively the 3WM and 4WM flux-tunable nonlinear coefficients, indicating the rates at which the corresponding interaction manifests, Φ_0 is the magnetic flux quantum, $R_Q = h/4e^2$, and $Z = \sqrt{L/C_g}$ is the characteristic impedance of the transmission line, with L the flux-tunable inductance per unit cell and C_g the ground capacitance per unit cell. Effectively, Eq. 1.12 constitutes the circuit equivalent of nonlinear optics Eq. 1.7, thus showing how wave mixing process may arise in superconducting circuits.
The ratio r between the critical currents of the small and large Josephson junctions is chosen so that the flux dependent magnitudes of the second and third order nonlinearities g_3 and g_4 are anti-correlated, meaning that when one is at zero the other is maximum (see Fig. 1.5b). This allows to separately explore the two different wave mixing processes.
In this thesis, since we are using the device as a four-wave mixing reversed Kerr parametric amplifier, we operate at the 'half flux' condition, with $g_3 \to 0$ and maximally negative g_4.

Under this conditions, solving the set of coupled wave equations which describe the energy exchange between pump, signal and idler fields [16, 17], or resorting once again to the analogy with nonlinear optical fibers [13], yield the power gain for non-degenerate 4WM to be given by:

$$G = \cosh^2(gx) + \frac{\Delta k^2}{4g^2}\sinh^2(gx) \tag{1.13}$$

where x is the distance traveled along the TWPA, Δk is the total phase mismatch and g is the parametric gain coefficient, depending on the pump power P_0, on the phase mismatch Δk, and on the nonlinear parameter γ defined in [13]: $g = \sqrt{(\gamma P_0)^2 - (\Delta k/2)^2}$.
It can be shown that G is maximum when $\Delta k = 0$; whereas for poor phase matching g becomes imaginary and the gain scales quadratically with length rather than exponentially. This demonstrates, in our specific case, the fundamental importance of phase matching, as more generally discussed in the previous section.

For a four wave mixing TWPA, in particular, the phase mismatch can be expressed as the sum of two distinct contributions:

$$\Delta k = \Delta k_{dispersion} + \Delta k_{Kerr} \tag{1.14}$$

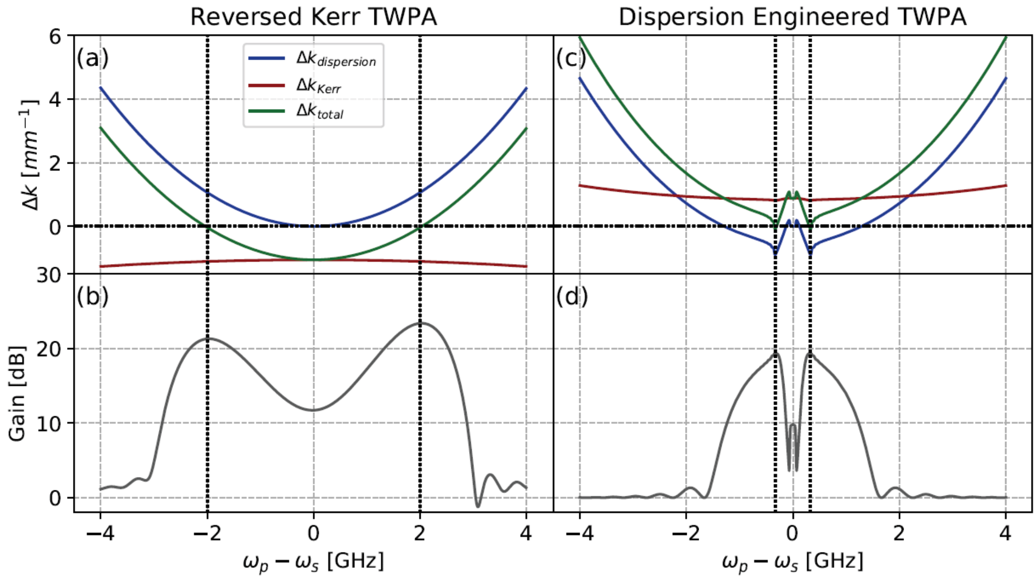

Figure 1.6: Simulations of reversed Kerr phase matching and gain (a and b) compared to dispersion engineering phase matching and gain (c and d) [18].
In (a) and (c), linear phase mismatch is represented by the blue line, Kerr phase mismatch by the red line (and characteristically it's negative in (a) and positive in (c)), and total phase mismatch by the green line. The gain maxima correspond, in both cases, to the frequencies with optimal phase matching.

where $\Delta k_{dispersion} = k_s + k_i - 2k_p$ is the linear phase mismatch, and $\Delta k_{Kerr} = 2\gamma P_0$ is the nonlinear phase mismatch, caused by third-order 'Kerr' phase modulation processes.
Usually, 4WM dispersion engineered TWPAs work in the regime of positive Kerr nonlinearity ($g_4 > 0$), and achieve phase matching by changing the sign of $\Delta k_{dispersion}$ through the strategies briefly exposed in the previous section. In the presented 'reversed Kerr' implementation, however, the same effect is obtained by operating the device in the regime of negative Kerr nonlinearity ($g_4 < 0$). Specifically, the reversed sign of the Kerr phase modulation, allows the total phase mismatch to vanish at two distinct signal frequencies, symmetrically on either side of the pump frequency. Two symmetric gain maxima are, therefore, observed in correspondence of these two frequencies.

Simulated comparison between reversed Kerr phase matching and traditional dispersion engineering phase matching, together with the respective expected gain profiles, is depicted in Fig. 1.6. As it can be seen in the diagrams, reversed Kerr phase matching effectively allows to reduce the ripples in the gain profile, typical of dispersion engineered TWPAs.
Also, since the sign reversal of the Kerr nonlinearity is not frequency dependent, the phase-matched amplification band can be dynamically tuned by simply changing the pump frequency, again with an advantage with respect to dispersion engineering phase matching.

Chapter 2

Axions and haloscopes

The axion [24, 25] is a beyond the Standard Model (BSM) hypothetical pseudo-scalar particle, first introduced in the seventies to solve the so-called strong CP problem, i.e. to explain why Parity (P) and Charge-conjugation Parity (CP) symmetries are conserved by strong interactions. If the axion mass were in the range of $1 - 100\,\mu$eV, the axion would also be a natural cold dark matter (CDM) candidate.

Traditionally, searches for dark matter candidates have focused on so-called weakly interacting massive particles (WIMPs). In recent years, however, with WIMP detectors improving their sensitivity to the point of nearly reaching the 'neutrino floor', we have witnessed a reduction in the available parameter space for WIMPs [26]. In addition, the search for these heavy candidates at high-energy colliders, such as LHC, has proved fruitless so far. Therefore, the axion is currently regarded as one of the most promising candidates for the constitution of cold dark matter, springing a proliferation of searches around the world.

Since axions are estimated to have a lifetime vastly greater than the age of the universe, and exceptionally weak interactions with matter and radiation, their detection has, however, proved to be extremely challenging.

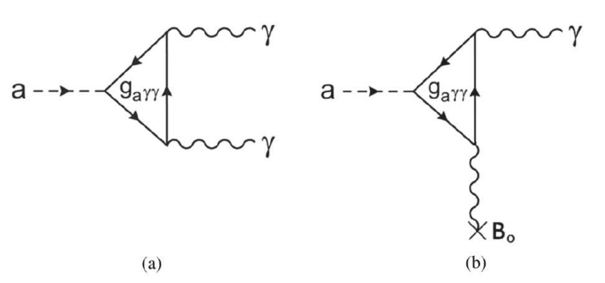

Figure 2.1: Feynman diagrams for axion decay into photons.
(a) Conversion of axion into two photons in vacuum.
(b) Inverse Primakoff effect in presence of an external magnetic field $\mathbf{B}_0$.

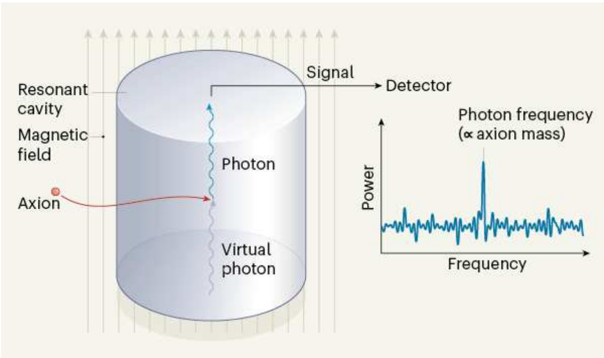

Figure 2.2: Schematic of an axion haloscope [27].
A potential axion enters a resonant microwave cavity, embedded in a strong magnetic field. As a result of the interaction in the cavity between the axion and a virtual photon, a real photon is generated. The resulting signal can be detected as an excess of power in the cavity at the photon frequency, proportional to the axion mass.

Most of the currently operating and proposed experiments rely on 'haloscopes', following a detection scheme proposed in 1983 by P. Sikivie. Axion detection in haloscopes exploits the so-called 'inverse Primakoff effect', in which the decay rate of axions to photons can be significantly increased in presence of a strong magnetic field [28].

The Lagrangian for the axion-photon interaction is given by:

$$\mathcal{L}_{a\gamma\gamma} = g_{a\gamma\gamma} a \, \mathbf{E} \cdot \mathbf{B} \tag{2.1}$$

where $g_{a\gamma\gamma}$ is the axion-photon coupling constant, proportional to the mass of the axion m_a, a is the axion field, and $\mathbf{E}$ and $\mathbf{B}$ are the electric and magnetic fields respectively. The coupling allows the axion to decay, in vacuum, into two photons, as shown in Fig. 2.1 (a). In presence of a static external magnetic field $\mathbf{B}_0$, instead, an axion may convert to a single photon, whose energy equals the total energy of the axion and it is, thus, directly related to the axion mass m_a. In this second configuration, shown in Fig. 2.1 (b), $\mathbf{B}$ in Eq. 2.1 is effectively substituted by static magnetic field $\mathbf{B_0}$. Consequently, as the external magnetic field strength is increased, so is the conversion rate of the axion.

A haloscope (see Fig. 2.2) consists of a high-Q microwave cavity permeated by a strong magnetic field, in which the described process is exploited to stimulate a resonant conversion of axions into photons. Specifically, when the cavity resonant frequency f_c is tuned to match the axion frequency $f_a = m_a c^2/h$, the power expected to be produced in the cavity is given by:

$$P_{a\rightarrow\gamma} \propto g_{a\gamma\gamma}^2 \frac{\rho_a}{m_a} B_0^2 V C_{mnl} Q_L \tag{2.2}$$

where m_a is the mass of the axion, ρ_a is the local mass density of the axion field, commonly assumed to be equal to the local dark matter density $\rho_{DM} \sim 0.4 - 0.45\,\mathrm{GeV/cm^3}$, B_0 is the magnetic field strength, V is the volume of the cavity, Q_L is the loaded quality factor of the cavity, and C_{mnl} is a form factor describing the overlap between the cavity mode electric field and the external magnetic field.
Typically expected values for P range between $10^{-24} - 10^{-23}\,\mathrm{W}$. The detection of such small powers is, clearly, one of the main challenges encountered in axion search.

2.1 Scan rate and noise temperature

The experimental technique we have described so far allows to probe axions having a well-defined mass m_a, determined by the cavity resonant frequency f_c. The axion mass, however, is unknown over a broad range. Consequently, haloscope cavities are designed to be tunable over a range of frequencies.

A critical figure of merit in this perspective is the 'scan rate', i.e. the mass range that can be explored within a certain amount of time, for a given sensitivity. More precisely, from Eq. 2.2 and simply using the well-known Dicke radiometer equation [29], it is possible to estimate the '*instantaneous* scan rate' for a haloscope. This latter parameter does not account for ancillary measurements and other data-taking related procedures, and, thus, determines the maximum speed at which the search over the frequency range can be conducted for a given signal-to-noise ratio (SNR).

Following [30], in presence of white gaussian Johnson noise, the Dicke radiometer equation relates the signal-to-noise ratio (SNR) to the axion signal power $P_{a\rightarrow\gamma}$:

$$\mathrm{SNR} = \frac{s}{n} = \frac{P_{a\rightarrow\gamma}}{k_B T_{sys}} \sqrt{\frac{t_m}{b}} \tag{2.3}$$

where T_{sys} is the system noise temperature defined in 1.6, k_B is Boltzmann's constant, b is the signal bandwidth, and t_m is the integration, i.e. observation, time.
In a haloscope, in particular, the input noise temperature T_{in} in Eq. 1.6 is given by the physical temperature of the resonant cavity T_{cav}. Precisely, in the classical regime of $k_B T_{cav} \gg h f_c$, we have that $T_{in} \approx T_{cav}$, whereas in the quantum regime, with $k_B T_{cav} \lesssim h f_c$, the relation between T_{cav} and T_{in} becomes:

$$T_{in} = \frac{h f_c}{2 k_B} \coth \frac{h f_c}{2 k_B T_{cav}} \tag{2.4}$$

with f_c being the cavity resonant frequency [31]. Also, for axion searches, typically SNR $> 3.5 - 5$, while the signal bandwidth b is given by

$$b = \frac{m_a}{Q_a} \tag{2.5}$$

where m_a is the axion mass, and $Q_a \approx 10^6$ is the axion 'quality factor', related to the kinetic energy distribution of dark matter particles in the galactic halo [32].

Combining Eqs. 2.3 and 2.5, and solving for t_m yield:

$$t_m = \mathrm{SNR}^2 \frac{(k_B T_{sys})^2}{P^2_{a\to\gamma}} \frac{m_a}{Q_a} \tag{2.6}$$

If we now assume the haloscope cavity loaded quality factor Q_L to be less than the axion quality factor Q_a, a number of signal bandwidths can be simultaneously scanned by the cavity. In these conditions, the time Δt required to scan over a small frequency range is

$$\Delta t = \frac{\Delta f}{Nb} t_m = \frac{\Delta f}{b} \left(\frac{Q_L}{Q_a}\right) t_m \tag{2.7}$$

where $N = Q_a/Q_L$ is the number of signal bandwidths that are being simultaneously scanned.

Finally, substituting Eqs. 2.2 and 2.6 into Eq. 2.7 and rearranging, yield the scan rate to be given by:

$$\frac{df}{dt} \approx \left(\frac{g^4_{a\gamma\gamma}}{\mathrm{SNR}^2}\right) \left(\frac{\rho_a^2 Q_a}{m_a^2}\right) \frac{B_0^4 Q_L (C_{mnl} V)^2}{(k_B T_{sys})^2} \tag{2.8}$$

In particular, since at fixed $g_{a\gamma\gamma}$ and at a specified target SNR, the instantaneous scan rate is given by

$$\frac{df}{dt} \propto \frac{1}{T^2_{sys}} \tag{2.9}$$

reducing the system noise temperature is an issue of critical importance for haloscope detectors. Specifically, the optimization of the system noise temperature via the combined use of dilution refrigerators and parametric amplifiers, can allow a scan rate improvement of a few hundredfolds compared to detection systems based on standard low-noise HEMT amplifiers.

Chapter 3

Characterization of QUAX's amplification chain

QUAX (QUaerere AXion) is an ongoing experiment at INFN's Legnaro National Laboratories, aimed at probing axion existence in a frequency region around 10 GHz [3, 33].
The experimental apparatus follows the standard 'haloscope' setup outlined in the previous chapter, and essentially consists of a cylindrical copper microwave cavity immersed in an 8 T magnetic field. The apparatus is equipped with a cryogenic and vacuum system, composed of a cryostat and a ^{3}He - ^{4}He wet dilution refrigerator. The cavity is located at lowest temperature stage of the refrigerator and its temperature is monitored by a RuO thermometer.
The rest of this thesis is dedicated to describing the characterization of the amplification chain of the apparatus, employing the reversed Kerr TWPA described in Chapter 1 as pre-amplifier.

3.1 Experimental Apparatus

The experimental setup can be essentially subdivided into two parts: a cryogenic section, comprising various components located at different temperature stages in the dilution refrigerator cryostat, and a room temperature section, comprising what will be referred to as 'room temperature electronics' (RTE). The schematic of both parts is reported in Fig. 3.1.

The TWPA is located, along with the copper cavity, at the lowest temperature stage ($T \approx 100$mK) of the cryostat.
The cavity mode that has been used for the measurements is the transverse magnetic mode TM030, with resonant frequency $f_{030} = 10.353531$ GHz [4].

The readout of the cavity is performed by means of a wire antenna (A1 in Fig. 3.1 (a)), whose coupling can be controlled with a mechanical feedthrough.
The output of the antenna is fed onto the amplification chain of the apparatus via the circulator C1. The amplification chain consists in the TWPA, serving as preamplifier, followed by a low-noise cryogenic HEMT amplifier, and by a room temperature HEMT amplifier. To prevent 'back-action' noise from the cryogenic HEMT, a pair of isolators (C2 and C3 in Fig. 3.1 (a)) and a 8 GHz High Pass filter are inserted between the TWPA and the cryogenic HEMT. We refer to this line as L4.
Access to the resonant cavity is also possible through a weakly coupled antenna, connected to the room temperature electronics (RTE) through line L1. This line employs a 12 dB attenuator to avoid contribution of thermal inputs from stages at higher temperatures than the system base temperature. An auxiliary line, L3 in figure, directly connects the RTE to the tunable antenna and the cavity, by means of circulator C1. This line is too equipped with attenuators to prevent thermal inputs, and is used both for providing a pump tone to the TWPA and for calibration purposes.
Finally, a DC current source is connected to a superconducting coil used to flux bias the TWPA.

Fig. 3.1 (b) schematizes the room temperature electronics. The setup employs two signal generators,

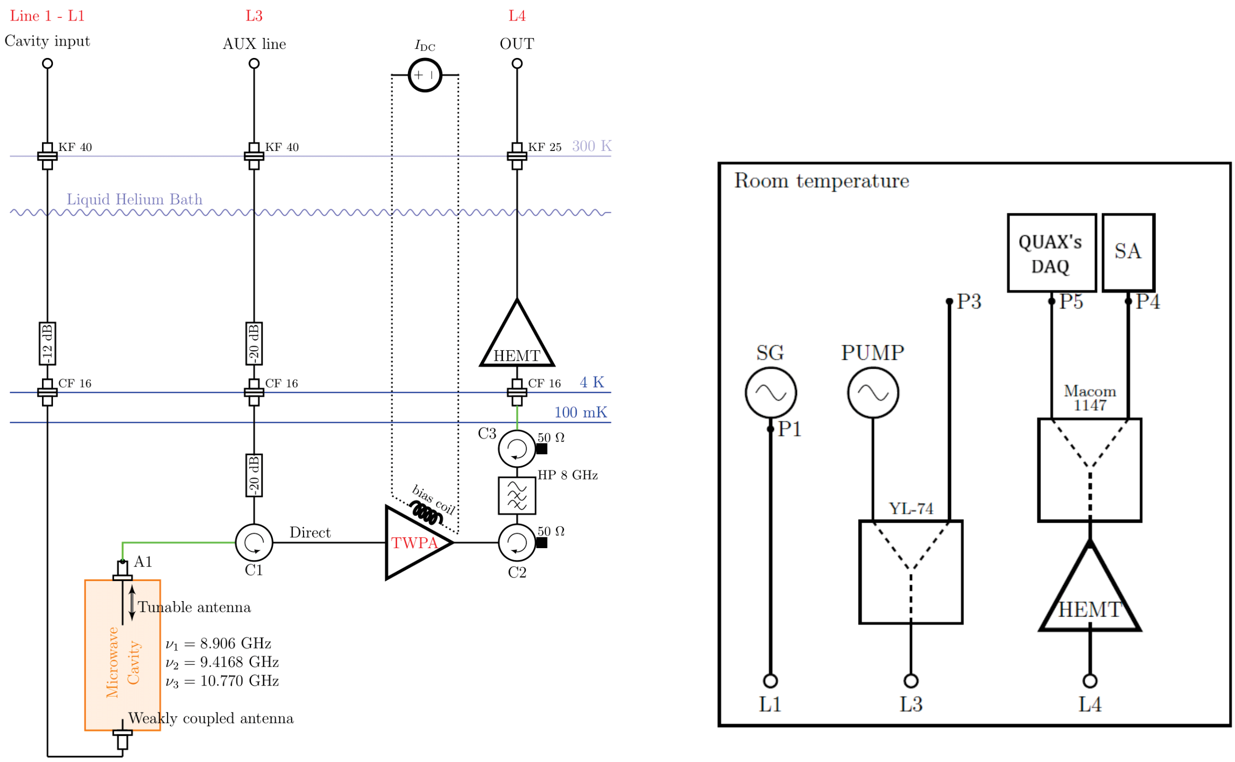

(a) Cryogenic apparatus (b) Room temperature electronics

Figure 3.1: Sketch of the analyzed experimental setup.
(a) Layout of the cryogenic apparatus: the point A1 is the reference point for the measurement of the system noise temperature.
(b) Room temperature radio frequency instrumentation: the points Pn are the reference points used in the measurements. L1, L3 and L4 are connected to the corresponding points in (a). SG and SA are respectively the signal generator and the spectrum analyzer, used for the system characterization. PUMP is a signal generator used to pump the TWPA. The box labeled as QUAX's DAQ denotes the experiment's data acquisition system, to be used for axion search, and consisting in a standard heterodyne detector (thus comprising a local oscillator, a mixer, and a ADC).

denoted as SG and PUMP, and a spectrum analyzer, denoted as SA.
PUMP is used to provide the pump tone to the parametric amplifier via line L3.
SG is used to provide a known input signal to the system, to be used for the apparatus characterization. Consequently, it can be moved between points P1, to provide an input on L1, and P3, to provide an input on L3. In the latter configuration, the signals generated by PUMP and SG are combined by a combiner before being sent to the cryogenic section of the apparatus.
The spectrum analyzer (SA) is used to read the output signals. For the characterization of the detection chain, it will be moved between points P4, to read the output on line L4, and P1, to read the output on line L1.
Finally, in the current experimental configuration, a power splitter on line L4 allows the output from the cavity to be simultaneously read by the spectrum analyzer and the Quax Data Acquisition apparatus. To the presented characterization, however, the reading through the SA is sufficient.

3.2 Measurements

3.2.1 Optimization of TWPA working point

The first measurements to be performed are aimed at optimizing the TWPA working parameters, namely: flux bias, pump frequency, and pump amplitude.

A first, raw, estimation of the optimal biasing current driving the superconducting coil, corresponding to the optimal flux bias, can be obtained by measuring the electronic chain transmission from point

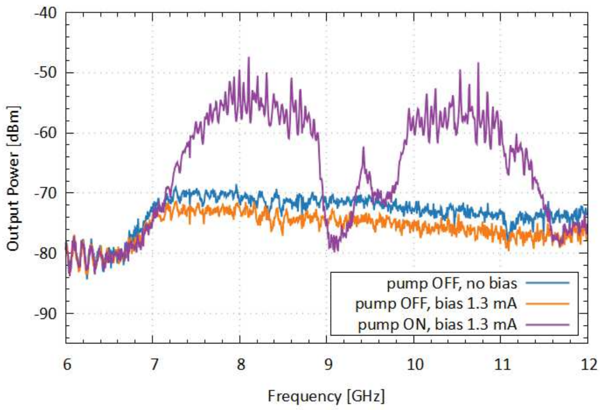

(a) Output spectra P3 → P4

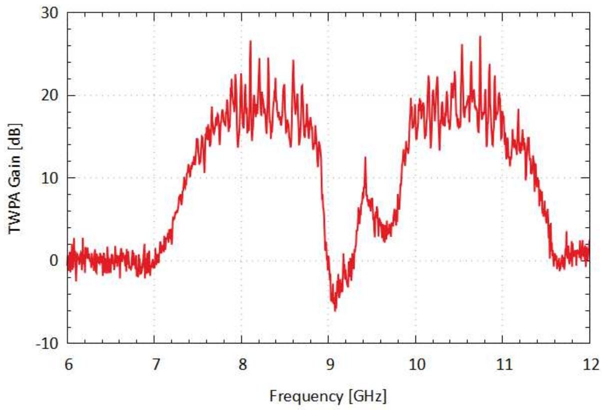

(b) TWPA gain estimate

Figure 3.2: Broad-band gain profile for the TWPA at the identified working point:
DC current bias $I_{DC} = 1.32\,\text{mA}$, pump frequency $f_P = 9.4181\,\text{GHz}$, pump amplitude $I_P = -81\,\text{dBm}$.
(a) Output spectra at P4 with and without DC current bias, and with and without pump tone. (b) TWPA gain, as obtained by subtracting the output spectrum in (a) with pump OFF from that with pump ON, with both spectra at 'half flux' bias.

P3 to point P4 while varying the DC current I_{DC} in the coil. The typical transmission presents some spurious modes, ascribable to spurious parametric interactions, periodically oscillating with the flux. The optimal flux bias for reversed Kerr amplification is found at the minima of such spurious modes oscillations. This corresponds to the 'half flux' condition defined in Chapter 1.
In the studied apparatus, minima were found with a periodicity of about 4 mA. Also, in contrast with theoretical expectations in ideal conditions, they were found to be slightly asymmetric around zero, due to the presence of a residual magnetic field originated from circulators C1 and C3, located close to the TWPA.
Among the different possible working points, the one featuring minimum current, amounting to $I_{DC} =$ 1.32 mA, was selected.

After choosing a proper flux bias, the amplifier can be driven with a pump. Since in reversed Kerr phase matching the pump frequency is not fixed by design, pump frequency and amplitude are determined by the frequency of the signal to be studied.
Remembering the characteristic two-lobed gain profile of a reversed Kerr TWPA (shown in Fig. 1.6), the pump frequency f_P is chosen so that the signal frequency corresponds to one of the two gain maxima. Whereas in an ideal lossless TWPA the behavior at either of the two maxima would be identical, asymmetric losses experienced by waves traveling at different frequencies cause the lower frequency maximum to be generally noisier [18]. In practice, it is thus preferable to work at the higher frequency maximum. This is achieved by setting the pump frequency lower than that of the signal.
Finally, the pump power level I_P is chosen by reducing of some fraction of a dB the value showing a saturation in the gain profile.
In our case, with the cavity mode of interest at $f_{030} \approx 10.35$ GHz, suitable values for the pump frequency and amplitude were found to be $f_P = 9.4181$ GHz and $I_P = -81$ dBm, where I_P must be intended as the pump amplitude at the input of the device.

The results of the described optimization procedure of the TWPA working parameters are displayed in Fig. 3.2.
Fig. 3.2a shows the output spectra recorded in P4 while sending from P3 an input power of $-130\,\text{dBm}$, normalized at 10.3 GHz in three different working conditions, namely:

- without providing nor flux bias nor a pump tone to the TWPA
- providing flux bias only, with $I_{DC} = 1.32$ mA, to the TWPA
- providing both flux bias, with $I_{DC} = 1.32$ mA, and a pump tone, with $f_P = 9.4181$ GHz and

$I_P = -81$ dBm, to the TWPA

The comparison between the output spectra in the first two configurations allows to appreciate in practice how the 'half flux' bias condition corresponds to a local minimum for the transmission parameter S43, corresponding to a minimum intensity for spurious parametric interactions.

On the other side, the comparison between the output spectra in the latter two configurations allows to estimate the power gain of the TWPA, as the ratio between the output spectra obtained with the PUMP generator turned ON and OFF respectively. The result is displayed in Fig. 3.2b and reproduces quite accurately the expected two-lobed shape.

It has to be noted that this, actually, is only an upper limit for the TWPA gain. The actual gain would be, in fact, measured with respect to the configuration where the TWPA is removed from the amplification chain and substituted by a quasi-lossless line, rather than with respect to the configuration where the PUMP generator is turned off.
This could, for example, be achieved using a pair of switches, which are not present in the current setup. Also, the addition of switches would allow to more accurately estimate TWPA losses in the linear regime, i.e. when no pump tone is applied, which we are implicitly neglecting in our model of the detection line. In particular, as shown in [18], TWPA losses are expected to be higher at higher frequencies, and we may estimate them to be in the order of a few dBs at our working frequency $f_{030} \sim 10$ GHz, thus not strictly negligible.
In any case, the exact calculation of the TWPA gain is not in general necessary to the characterization of the detection apparatus, since the only truly fundamental figure of merit needed to characterize the signal strength is the gain of the complete detection chain of the haloscope.

Finally, once the optimal pump amplitude and frequency have been determined, the determination of the TWPA working point can be further improved by a fine tuning of the flux bias around the previously determined biasing current. Once again, this is done by measuring the line transmission from point P3 to point P4 and trying to optimize the gain in a more limited frequency range, about the cavity resonance. The implementation of this strategy yielded an optimized biasing current of $I_{DC} = 1.378$ mA

3.2.2 Line gains and Noise Temperatures

Once the TWPA is correctly in operation, it is possible to proceed to the characterization of the apparatus. The characterization consists in estimating the effective gain and noise temperature of the overall detection chain from the cavity output (A1) to the point P4.
This is achieved by injecting calibrated signals, via the signal generator SG, along lines L1 and L3, and contextually measuring, via the spectrum analyzer SA, the output spectra at points P1 and P4, following a method first introduced in [34]. This method, described in the following, allows to measure the system noise temperature exactly at the point of interest, i.e. the cavity output, and does not require the employment of switches or calibrated noise sources.

Specifically, we measure the following three transmission power spectra:

- S41: Transmission from point P1 to point P4
- S43: Transmission from point P3 to point P4
- S13: Transmission from point P3 to point P1

The power output P_{out}^{xy} read by the spectrum analyzer at point Py, when the signal generator injects from Px a pure tone of power P_{in} is given by:

$$P_{out}^{xy} = P_n^{xy} + G_{xy} \cdot P_{in} \qquad (xy) = \{14,\ 34,\ 13\} \tag{3.1}$$

where P_n^{xy} is the noise power at the spectrum analyzer and G_{xy} is the overall line gain from point Px to point Py, at the input frequency.
Since we are interested in the behavior of the detection chain at cavity resonance, all measurements,

with the exception of spectrum S43, are performed with input signals at the resonant frequency of the mode of interest: $f_{030} = 10.353731\,\text{GHz}$. In the case of S43, where the measured transmission happens in reflection with respect to the cavity, rather than in transmission through the cavity, as for S41 and S13, a slightly detuned frequency is used, just off resonance. This allows to prevent unwanted absorption of input signal power by the cavity.
Also, all measurements are performed with the tunable antenna almost critically coupled to the cavity.

Using Eq. 3.1, we can readily estimate the parameters G_{xy} and P_n^{xy} for each of the three possible configurations - S41, S43, and S13 - by measuring the power outputs P_{out}^{xy} for a given set of power inputs P_{in}, and performing a straight line fit of the collected data.

We can also define the following, frequency dependent, line gains down to the common reference point given by the tunable antenna (A1):

- g_1: gain from the point P1 to the antenna A1 (bidirectional)
- g_3: gain from the point P3 to the antenna A1 (bidirectional)
- g_4: gain from the antenna A1 to the point P4

Clearly, the line gains G_{xy} defined in Eq. 3.1 are related to g_1, g_2, g_3 by $G_{xy} = g_x \cdot g_y$, with $(xy) = \{14,\, 34,\, 13\}$. Inverting these three relations yields:

$$g_1 = \sqrt{\frac{G_{14}G_{13}}{G_{34}}} \qquad g_3 = \sqrt{\frac{G_{34}G_{13}}{G_{14}}} \qquad g_4 = \sqrt{\frac{G_{14}G_{34}}{G_{13}}} \tag{3.2}$$

In particular, g_4 represents the effective gain of the complete detection chain, from the antenna to the Data Acquisition electronics, and it is, therefore, the parameter of physical interest to the characterization of the apparatus.

Once the gain g_4 is known, the equivalent system noise temperature T_{sys} of the detection chain, at the antenna point A1, can be inferred from spectra S41 and S43, i.e. the ones carrying the information about the amplification chain, using that noise power at the spectrum analyzer can be written as:

$$P_n^{xy} = g_4 k_B T_{sys} B + \text{Noise}_{\text{SA}} \qquad (xy) = \{14,\, 34\} \tag{3.3}$$

where k_B is Boltzmann's constant, and B and Noise_{SA} are the spectrum analyzer's resolution bandwidth and noise floor respectively.

3.3 Results

P_{in} (dBm)	P_{out} (pW) $f_c - 200$kHz	P_{out} (pW) $f_c + 200$kHz
off	128.3	116.8
-99	172.1	168.9
-98	176.7	177.9
-95	247.6	228.4
-94	250.0	253.7
-92	334.5	329.3
-91	389.2	398.8
-90	468.0	430.3

(a) S43

P_{in} (dBm)	P_{out} (fW) B = 100kHz	P_{out} (fW) B = 30kHz
off	101.7	30.05
10	166.9	96.08
11	182.4	112.5
12	209.2	128.1
13	226.4	157.0
14	263.2	185.8
15	301.6	228.6

(b) S13

P_{in} (dBm)	P_{out} (pW)
off	112.5
-90	152.8
-89	164.3
-88	168.4
-87	183.0
-84	257.9
-82	330.4
-80	480.0

(c) S41

Table 3.1: Experimental data (a) Transmission spectrum S43: two columns contain the data obtained at 200 kHz below and above the cavity resonance frequency $f_c = f_{030}$ respectively. (b) Transmission spectrum S13: two columns contain the data obtained with a resolution bandwidth of 100 kHz and 30 kHz respectively. (c) Transmission spectrum S41.

Table 3.1 contains the experimentally collected data for the transmission power spectra S43, S13 and S41.

The data acquisition was conducted in absence of the strong magnetic field required in axions searches. However, the setup is already equipped with magnetic shielding; thus, the system behavior is not expected to vary much once the apparatus will be set up as an operating haloscope.
The cavity temperature during data acquisition operations was $T_{cav} \approx 110 - 115\,\mathrm{mK}$, as measured by the RuO thermometer.
The noise floor of the spectrum analyzer is $\mathrm{Noise}_{\mathrm{SA}} = 100$ fW, thus virtually negligible compared to the measured noise powers.
The resolution bandwidth of the spectrum analyzer was set to $B = 100\,\mathrm{kHz}$ for spectra S41 and S43. For spectrum S31, since the output power level to be measured was extremely weak - the input signal does not go through the amplification chain in this configuration - an additional measurement with a smaller bandwidth $B = 30\,\mathrm{kHz}$ was performed. Finally, for S43, given the necessity to operate at a slightly detuned frequency with respect to the cavity resonance, two sets of measurements were acquired, corresponding to frequencies shifted 200 kHz above and below resonance respectively.

Following the scheme laid out in the previous section, straight line fits were performed on the data reported in Tab. 3.1.
Figure 3.3 shows the results of these fits.

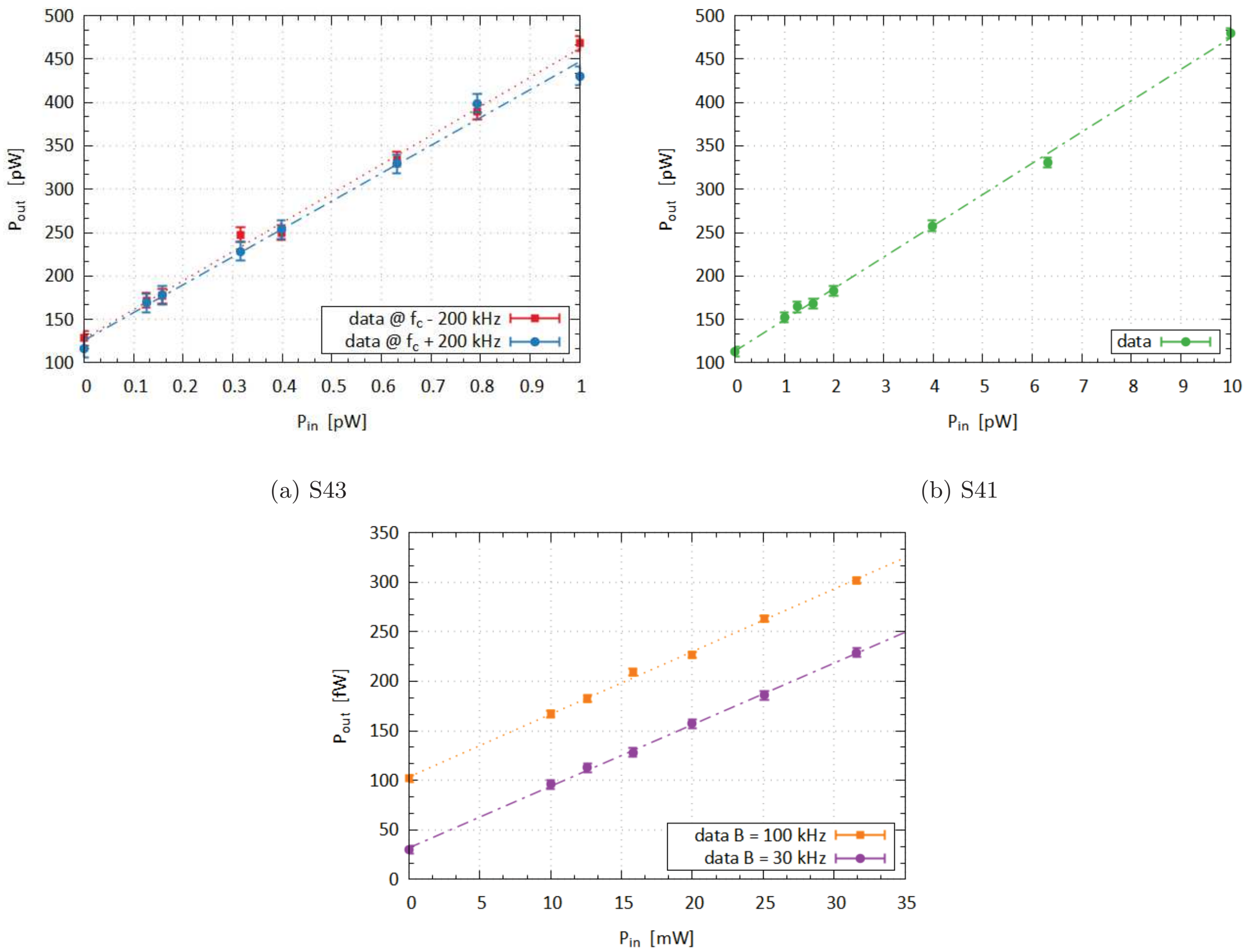

(a) S43 (b) S41

(c) S31

Figure 3.3: Least squares linear fits to the experimental point for each transmission spectrum.

In all cases the experimental data seem to conform well to the linear relation predicted by Eq. 3.1. Also, the obtained fit intercepts are always well compatible with the measured points with no input

power, denoted as 'off' in Tab. 3.1.
The parameters returned by the fits are reported in Table 3.2.
For spectrum S43, where two sets of data were available, two fits were performed. After having verified their reciprocal compatibility, the results obtained from each fit were averaged to obtain the parameters G_{34} and P_n^{34} displayed in Tab. 3.2. Similarly, for spectrum S31, the reported gain G_{13} is the average of the gains obtained from fitting the two sets of data with different resolution bandwidths. In this case, the ratio between the two fit intercepts, i.e. the noise powers P_n^{13} at the spectrum analyzer, was found to be approximately equal to the ratio between the two resolution bandwidths, in accordance with the theoretical expectation $P_n \propto B$.
The errors on the parameters reported in Tab. 3.2 are those obtained by the fits. The error on each measured point, instead, is essentially determined by the number of averages performed by the spectrum analyzer in the acquisition. Since this setting was left unchanged during the whole data acquisition, all measured points effectively have the same error. This justifies to perform simply a least-squares fit.

From the parameters in Tab. 3.2, using Eq. 3.2 and 3.3 one can calculate the parameters of interest to the characterization of the apparatus. The results are shown in Table 3.3.

G_{34}	328 ± 7
G_{14}	36.1 ± 0.6
G_{13}	$(6.3 \pm 0.1) \times 10^{-12}$
P_n^{34}	$(1.27 \pm 0.04) \times 10^{-10}$ W
P_n^{14}	$(1.13 \pm 0.03) \times 10^{-10}$ W
P_n^{13} (B = 100kHz)	$(10.3 \pm 0.2) \times 10^{-12}$ W
P_n^{13} (B = 30kHz)	$(3.1 \pm 0.2) \times 10^{-12}$ W

Table 3.2: Results obtained from the fits displyed in Fig. 3.3.

g_1	$(8.3 \pm 0.1) \times 10^{-7}$
g_3	$(7.6 \pm 0.1) \times 10^{-6}$
g_4	$(4.32 \pm 0.08) \times 10^{7}$
T_{sys}^{34}	(2.12 ± 0.07)K
T_{sys}^{14}	(1.90 ± 0.06)K

Table 3.3: Inferred values for physically relevant parameters.

As discussed in the previous section, both spectra S43 and S41 carry information on the noise level of the system. The corresponding estimates of the system equivalent noise temperature, T_{sys}^{34} and T_{sys}^{14} respectively, are in agreement within $2.4\,\sigma$. Thus, a final estimate for the system noise temperature can be taken as the average between the two individual estimates. Together with the total line gain g_4, this completes the characterization of the detection chain at the operating frequency, yielding:

$$g_4(\text{dB}) = (76.4 \pm 0.1) \text{ dB} \qquad T_{sys} = (2.01 \pm 0.06) \text{ K} \tag{3.4}$$

where we have taken a conservative error on the noise temperature. This choice accounts both for the recorded dispersion between the two estimates obtained from S43 and S41 respectively, and for the expected temporal fluctuations, possibly present if the apparatus is not strictly time-stationary.

Comparing the recorded system noise temperature to the one given by standard quantum limit (SQL) at $f \approx 10\,$GHz:

$$T_{sys}^{SQL} = \frac{hf}{k_B} = 0.5 \text{ K} \tag{3.5}$$

yields that the analyzed amplification chain is about four times noisier than SQL. Since the TWPA itself is expected to be working at a temperature about twice as high as SQL [18], we conclude that the analyzed detection line, while setting a record low value for a wide-band amplification chain at ~ 10 GHz frequencies, can possibly be improved to performances closer to SQL.
For instance, a possible cause of the observed excess noise power may hold in residual thermal inputs, originated at higher temperature stages and reaching the cavity output through line L3. In this hypothesis, an optimization of the attenuators arrangement in the line could help reach lower noise temperatures.

The estimation of the detection line gain g_4 and of the system noise temperature T_{sys} effectively concludes the characterization of the detection chain.

However, given the parameters reported in Tab. 3.3 and knowing the characteristics of the other components of the amplification chain, we may also try to estimate the gain and the noise temperature of the TWPA alone, G_{TWPA} and T_{TWPA} respectively.

The nominal gains of the two HEMTs employed in the amplification chain are 37 dB and 35 dB for the cryogenic and room temperature ones respectively. The noise temperature of the cryogenic HEMT, as previously measured on a different setup, is $T_{\text{HEMT}} = (4.5 \pm 0.5)$ K. The cable losses in the cryogenic section are estimated to be $\Lambda_1 = 0.3$ dB from the antenna A1 to the TWPA input, and $\Lambda_2 = 0.7$ dB from the TWPA to the cryogenic HEMT, while a total lines loss of 20 dB is expected for the complete detection chain.

By combining the information about HEMT gains and line losses with the measured total line gain $g_4 = 76.4$ dB, one can estimate the gain of the parametric amplifier to be $G_{\text{TWPA}} \approx 24$ dB, in accordance both with the theoretical expectations, shown in Fig. 1.6, and with previously presented experimental results, shown in Fig. 3.2b.

On the other side, adapting Eqs. 1.6 and 1.2 to the analyzed amplification chain, and taking into account line losses as well as amplifier gains, yield:

$$T_{sys} \approx \frac{h\nu_c}{2k_B} \coth \frac{hf_c}{2k_B T_{cav}} + \Lambda_1 T_{\text{TWPA}} + \frac{\Lambda_2 \Lambda_1}{G_{\text{TWPA}}} T_{\text{HEMT}} \tag{3.6}$$

where the first term represents the cavity equivalent noise temperature, including vacuum 'zero-point' fluctuations, as given by Eq. 2.4. $T_{cav} \approx 110\,\text{mK}$ and $f_c = f_{030} \approx 10.35\,\text{GHz}$ are the cavity's physical temperature and resonant frequency respectively.
From Eq. 3.6 we can estimate the TWPA equivalent noise temperature at the operating frequency to be $T_{\text{TWPA}} = (1.8 \pm 0.1)\,\text{K}$. This estimate includes both the input noise at the idler frequency, comprising vacuum fluctuations and potentially thermal ones, and the intrinsic excess noise of the amplifier, which would be equal to zero in the Standard Quantum Limit.
Also, Eq. 3.6 allows to appreciate once again the fundamental importance for the TWPA gain to be large enough to suppress noise contributions from following stages in the amplification chain, with the HEMT in the first place. By comparing the estimated equivalent noise temperatures T_{sys}, T_{TWPA} and T_{HEMT}, of the complete amplification chain, the TWPA and the HEMT respectively, we can conclude that this seems to be the case in the analyzed detection chain.

As previously noticed, the obtained values for G_{TWPA} and T_{TWPA} must be thought merely as a rough estimate of the device's actual behavior. More reliable and accurate estimates of the individual figures of merit characterizing each constituent element in the detection chain - and the TWPA in particular - require in fact a precise knowledge of TWPA losses in the linear regime, which could not be achieved in the present setup.

Conclusions

In this work we have described and performed the characterization of an amplification chain to be used in the search of dark matter axions.
The analyzed amplification chain is based on a JTWPA exploiting a reversed Kerr phase-matching mechanism, which is employed as preamplifier in the readout of a 3D microwave resonant cavity. The studied apparatus is part of the experiment QUAX, aimed at probing axion existence around 10 GHz within a 'haloscope' setup, and will be at the core of the forthcoming experiment's data taking runs. JTWPAs in general, on the other side, are likely set to become a ubiquitous tool for a broad range of experiments and technologies in the field of circuit QED.

The presented characterization procedure allows to precisely measure the system equivalent noise temperature exactly at the relevant measurement point (i.e. the cavity output) and does not require the use of calibrated noise sources nor switches.
A gain of (76.4 ± 0.1) dB and a system noise temperature of (1.97 ± 0.06) K were measured at a frequency of ~ 10.35 GHz.

Despite being about four times higher than Standard Quantum Limit, the recorded noise temperature represents a significant achievement for a wide-band amplifier at the studied high frequencies, and is suitable for axion detection at a haloscope.
The prospect of improving the obtained result, which would translate into a faster scan of the axion-photon interaction parameter space, could be investigated using a modified setup. For instance, an optimization of the attenuators employed in the apparatus could to help further prevent potential thermal inputs from higher temperatures, whereas the addition of a pair of switches would allow a better understanding of TWPA losses in linear regime.

Bibliography

[1] Jose Aumentado. “Superconducting Parametric Amplifiers: The State of the Art in Josephson Parametric Amplifiers”. In: *IEEE Microwave Magazine* 21.8 (2020), pp. 45–59.

[2] P. Krantz et al. “A quantum engineer’s guide to superconducting qubits”. In: *Applied Physics Reviews* 6.2 (2019), p. 021318.

[3] Riccardo Barbieri et al. “Searching for galactic axions through magnetized media: the QUAX proposal”. In: *Physics of the Dark Universe* 15 (2017), pp. 135–141.

[4] D. M. Pozar. *Microwave Engineering.* John Wiley & Sons, 2004.

[5] C. M. Caves. “Quantum limits on noise in linear amplifiers”. In: *Phys. Rev. D* 26 (1982).

[6] R. B. Boyd. *Nonlinear Optics, 3rd ed.* San Diego: Academic Press, 2008.

[7] M. Malnou et al. “Three-Wave Mixing Kinetic Inductance Traveling-Wave Amplifi er with Near-Quantum-Limited Noise Performance”. In: *PRX Quantum* 2.10302 (2021).

[8] B. D. Josephson. “Possible new effects in superconducting tunneling”. In: *Phys. Lett.* 1 (1962).

[9] M. A. Castellanos-Beltran and K. W. Lehnert. “Widely tunable parametric amplifier based on a superconducting quantum interference device array resonator”. In: *Applied Physics Letters* 91.083509 (2007).

[10] M. A. Castellanos-Beltran et al. “Amplification and squeezing of quantum noise with a tunable Josephson metamaterial”. In: *Nature Physics* 4 (2008).

[11] B. Yurke et al. “Observation of 4.2-K equilibrium-noise squeezing via a Josephson-parametric amplifier”. In: *Phys. Rev. Lett.* 60 (1988).

[12] B. Yurke et al. “Observation of parametric amplification and deamplification in a Josephson parametric amplifier”. In: *Phys. Rev. A* 39 (1989).

[13] G. Agrawal. *Nonlinear fiber optics, 3rd ed.* San Diego: Academic Press, 2001.

[14] L. Planat et al. “Photonic-Crystal Josephson Traveling-Wave Parametric Amplifier”. In: *Phys. Rev. X* 10.021091 (2020).

[15] C. Macklin et al. “A near quantum-limited Josephson traveling-wave parametric amplifier”. In: *Science* 350 (2015).

[16] K. O’Brien et al. “Resonant phase matching of josephson junction traveling wave parametric amplifiers”. In: *Phys. Rev. Lett.* 113 (2014).

[17] M. T. Bell and A. Samolov. “Traveling-Wave Parametric Amplfi er Based on a Chain of Coupled Asymmetric SQUIDs”. In: *Phys. Rev. Appl.* 4.024014 (2015).

[18] Arpit Ranadive et al. “Kerr reversal in Josephson meta-material and traveling wave parametric amplification”. In: *Nature Communications* 13.1737 (Apr. 2022).

[19] NE Frattini et al. “3-wave mixing Josephson dipole element”. In: *Applied Physics Letters* 110.22 (2017), p. 222603.

[20] NE Frattini et al. “Optimizing the nonlinearity and dissipation of a snail parametric amplifier for dynamic range”. In: *Physical Review Applied* 10.5 (2018), p. 054020.

[21] VV Sivak et al. “Kerr-free three-wave mixing in superconducting quantum circuits”. In: *Physical Review Applied* 11.5 (2019), p. 054060.

[22] VV Sivak et al. “Josephson array-mode parametric amplifier”. In: *Physical Review Applied* 13.2 (2020), p. 024014.

[23] Alexander Grimm et al. “Stabilization and operation of a Kerr-cat qubit”. In: *Nature* 584.7820 (2020), pp. 205–209.

[24] Francesca Chadha-Day, John Ellis, and David J. E. Marsh. "Axion dark matter: What is it and why now?" In: *Science Advances* 8.8 (2022), eabj3618.

[25] Yannis K. Semertzidis and SungWoo Youn. "Axion dark matter: How to see it?" In: *Science Advances* 8.8 (2022), eabm9928.

[26] J. Beringer et al. "Review of Particle Physics". In: *Phys. Rev. D* 86 (1 July 2012), p. 010001.

[27] Igor G. Irastorza. "Shedding squeezed light on dark matter". In: *Nature* 560 (2021), pp. 226–227.

[28] H. Primakoff. "Photo-Production of Neutral Mesons in Nuclear Electric Fields and the Mean Life of the Neutral Meson". In: *Phys. Rev.* 81 (5 Mar. 1951), pp. 899–899.

[29] R. H. Dicke. "The Measurement of Thermal Radiation at Microwave Frequencies". In: *Review of Scientific Instruments* 17.7 (1946), pp. 268–275.

[30] I Stern et al. "Cavity design for high-frequency axion dark matter detectors". In: *Review of Scientific Instruments* 86.12 (2015), p. 123305.

[31] Slawomir Simbierowicz et al. "Characterizing cryogenic amplifiers with a matched temperature-variable noise source". In: *Review of Scientific Instruments* 92.3 (2021), p. 034708.

[32] Michael S. Turner. "Periodic signatures for the detection of cosmic axions". In: *Phys. Rev. D* 42 (10 Nov. 1990), pp. 3572–3575.

[33] D. Alesini et al. "Search for invisible axion dark matter of mass $\mathrm{m}_a = 43\ \ \mu\mathrm{eV}$ with the QUAX–$a\gamma$ experiment". In: *Phys. Rev. D* 103 (10 May 2021), p. 102004.

[34] N. Crescini et al. "Axion Search with a Quantum-Limited Ferromagnetic Haloscope". In: *Phys. Rev. Lett.* 124 (17 May 2020), p. 171801.